Advanced Functional Materials

ADVANCED FUNCTIONAL MATERIALS
www.afm-journal.de

RESEARCH ARTICLE

Stress-Triggered Ionic Rearrangement Produces Self-Strengthening Eutectogels With Decoupled Mechanical Rigidity and Ionic Conductivity

Yongzhi Liang[1,2] | Lulu Yin[1] | Zengbai Ouyang[1] | Lingyu Zhao[1] | Jinsong Leng[3]

[1]Department of Materials Science and Engineering, Southern University of Science and Technology, Shenzhen, China | [2]School of Science, Harbin Institute of Technology, Shenzhen, China | [3]Center for Composite Materials and Structures, Harbin Institute of Technology, Harbin, China

Correspondence: Yongzhi Liang (lyz12@mail.ustc.edu.cn) | Lingyu Zhao (zhaoly@sustech.edu.cn) | Jinsong Leng (lengjs@hit.edu.cn)

Received: 1 February 2026 | **Revised:** 2 April 2026 | **Accepted:** 25 May 2026

Keywords: eutectogels | flexible Sensors | self-strengthening | stress-triggered rearrangement | ultra-robustness

ABSTRACT

High-performance conductive gels possess exceptional mechanical robustness yet exhibit compromised ductility, conductivity, and self-reinforcement capability, owing to the impeded ion transport and restricted dynamic reconstruction within dense networks. This dilemma is overcome here by a stress-triggered ionic rearrangement strategy that exploits the dynamic reorganization of mobile ions to decouple ionic conductivity from structural rigidity. This strategy engineers a network saturated with dispersed free ions to guarantee superior conductivity independent of structural density, triggers in situ aggregation of these ions into high-density ionic cross-linking domains upon deformation, and consequently activates a potent self-strengthening mechanism that reaches a maximum of 185% of the initial value. Consequently, this structural evolution translates into an unprecedented convergence of mechanical robustness and functional agility, yielding a tensile strength of 34.58 MPa, an elastic modulus of 77.38 MPa, and a volumetric toughness of 177.3 MJ/m^3. Crucially, such extreme mechanical reinforcement is achieved without compromising the dynamic nature, preserving a high extensibility of 644.5% alongside efficient ionic conductivity. Leveraging this unique material platform, we develop a flexible sensor with a detection limit of 10 μm. The sensor demonstrates precise recognition of diverse physiological activities, from large-scale limb movements to subtle signals such as swallowing, pulse, and respiration.

1 | Introduction

Conductive gels, characterized by their unique integration of tissue-like softness, biocompatibility, and efficient ionic/electronic transport capabilities, constitute the fundamental building blocks of next-generation flexible bio-electronics, neural interfaces, and soft robotics [1–5]. As human–machine interaction technologies expand in both depth and scope, the application scenarios for these materials are undergoing a fundamental paradigm shift, moving from superficial physiological monitoring to complex, load-bearing structural components (e.g., artificial tendons, biomechanical prosthetics, and mechanically adaptive skins) [2, 6, 7]. Specifically, this functional transition necessitates the synergistic incorporation of electrical and mechanical engineering, which endows the materials with high sensitivity for precisely capturing minute physiological electrical signals while simultaneously guaranteeing ultra-high mechanical robustness capable of matching or even exceeding that of natural load-bearing tissues [8, 9]. However, unifying ultra-high strength, superior conductivity, and dynamic self-strengthening capability within a single polymer network remains an elusive scientific barrier in polymer physics [10, 11]. Current high-performance conductive gels face inescapable intrinsic trade-offs: (i) To

achieve high modulus and tensile strength, polymer networks typically require extremely high cross-linking densities or the introduction of rigid crystalline domains. Such dense microstructures inevitably compress the free volume and act as barriers to ion migration, causing electrical conductivity to decay exponentially as mechanical strength increases; (ii) Self-strengthening mechanisms rely on the dynamic reconstruction of the microstructure during deformation to counteract damage. Conversely, traditional ultrahigh-strength networks often lack sufficient chain mobility, once subjected to stress, they tend to succumb to catastrophic brittle fracture or irreversible plastic yielding, effectively precluding any constructive structural remodeling [12, 13].

To circumvent these performance bottlenecks, researchers have made substantial strides by introducing energy dissipation mechanisms. The classic double-network (DN) strategy exploits the rupture of sacrificial bonds to boost toughness [14, 15]. However, this approach is often plagued by significant mechanical hysteresis and softening effects [16, 17]. To address this issue, Zhu et al. proposed a topological design strategy based on a highly entangled network structure. By employing a "sliding" mechanism of physical entanglements as a substitute for chemical bond scission, they successfully reconciled the conflict between high toughness and low hysteresis [18]. Despite improving recoverability, the strategy's inherent reliance on physical entanglements results in an absolute strength (~3 MPa) that falls short of the rigorous demands for high-end structural materials. In the pursuit of ultimate strength, inspired by natural tendons, Kang et al. developed supramolecular interlocking anisotropic ionogels (ACIGs), achieving a directional tensile strength of up to 175 MPa through the incorporation of rigid fiber bundles [19]. While demonstrating the potential of ionic liquids for reinforcement, this strategy fundamentally relies on the introduction of extrinsic rigid phases. This dependence not only induces mechanical anisotropy but also compromises the uniform extensibility of the gel under large deformations due to the presence of rigid fibers, thereby constraining its applicability in omnidirectional sensing.

Beyond the pursuit of static ultimate strength, a more profound paradigm shift in this field lies in endowing materials with the capacity for 'adaptive self-strengthening' under deformation. While conventional strengthening strategies aim to passively delay failure, ideal self-strengthening materials upend this logic by transforming the destruction process into an opportunity for reinforcement [17, 20]. Wang et al. achieved a pioneering breakthrough in this direction by leveraging mechanochemistry [10]. They ingeniously utilized mechanoradicals generated from the scission of weak bonds as initiators to trigger rapid in situ polymerization of monomers at crack tips, inhibiting crack propagation via a 'destruction-induced construction' mechanism. However, while this strategy validates the concept of self-strengthening, it fails to fundamentally breach the absolute strength limit of hydrogels. Constrained by the inherent softness of the precursor network and the kinetic lag of new network formation, the ultimate tensile strength of such materials. Even after reinforcement, the gel typically remains at a low level (often <1 MPa). This falls far short of the ultra-high strength standards required for load-bearing structural applications (>10 MPa). Furthermore, the in situ formation of rigid polymer networks tends to obstruct ion migration pathways, rendering the simultaneous achievement of extreme mechanical strength and high electrical conductivity an unresolved challenge [21–23].

Addressing these multifaceted conflicts, we propose a strategy based on "Stress-Triggered Ionic Rearrangement" that successfully decouples structural rigidity from ionic conductivity, yielding high-performance conductive eutectogels endowed with combined ultrahigh strength and self-strengthening capabilities. Composed of an iron-ion-cross-linked polymer network solved in a deep eutectic solvent (DES), our design philosophy relies on a "dynamic-static separation" mechanism. In the initial state, the network is replete with abundant dispersed ions, guaranteeing superior electrical conductivity independent of the matrix density, upon tensile deformation, the initial iron-ion cross-links dissociate and undergo stress-induced dynamic rearrangement, in situ aggregating into higher-coordination configurations to form high-density strong ionic cross-linking domains. This unique dynamic structural evolution endows the eutectogel with a maximum 1.85-fold self-strengthening effect and realizes an unprecedented convergence of mechanical and electrical performance. It achieves a tensile strength of 34.58 MPa, an elastic modulus of 77.38 MPa, a volumetric toughness of 177.3 MJ/m^3, and an ultra-high extensibility of 644.5%, all while preserving excellent conductivity. Leveraging this platform, we developed a flexible sensor with a detection limit as low as 10 μm, capable of withstanding extreme mechanical loads while precisely recognizing diverse signals, ranging from large-scale limb movements to subtle physiological activities such as swallowing and respiration. This work not only transcends the performance limits of traditional polymer networks but also provides a novel paradigm for designing mechanically adaptive, next-generation intelligent soft materials.

2 | Results and Discussion

2.1 | Fabrication and Evolution of Mechanical Robustness

To overcome the intrinsic fragility of conventional gels and resolve the conflict between high strength and conductivity, we engineered a hierarchical network via a multi-step densification and solvent replacement strategy. The fabrication process and the corresponding structural evolution are schematically illustrated in Figure 1a. Initially, a transparent, non-ionic cross-linked poly(acrylamide-*co*-acrylic acid) hydrogel (denoted as NIC Hydrogel) was synthesized via UV-initiated polymerization. This precursor network possesses a loose, water-swollen topology dominated by weak hydrogen bond interactions, resulting in a soft and sticky matrix. Subsequently, the NIC Hydrogel was immersed in the Fe^{3+} solution, where the ferric ions coordinated with the carboxyl groups ($-COO^-$) on the polymer chains. This ionic coordination induced significant volume shrinkage and chain densification, transforming the material into an IC Hydrogel. Finally, the IC Hydrogel was soaked in a deep eutectic solvent (DES) to facilitate solvent exchange. The introduction of DES not only replaced water molecules but also reinforced the polymer network through extensive hydrogen bonding and electrostatic interactions, yielding the final IC Eutectogel with a stable, highly entangled, and conductive microstructure.

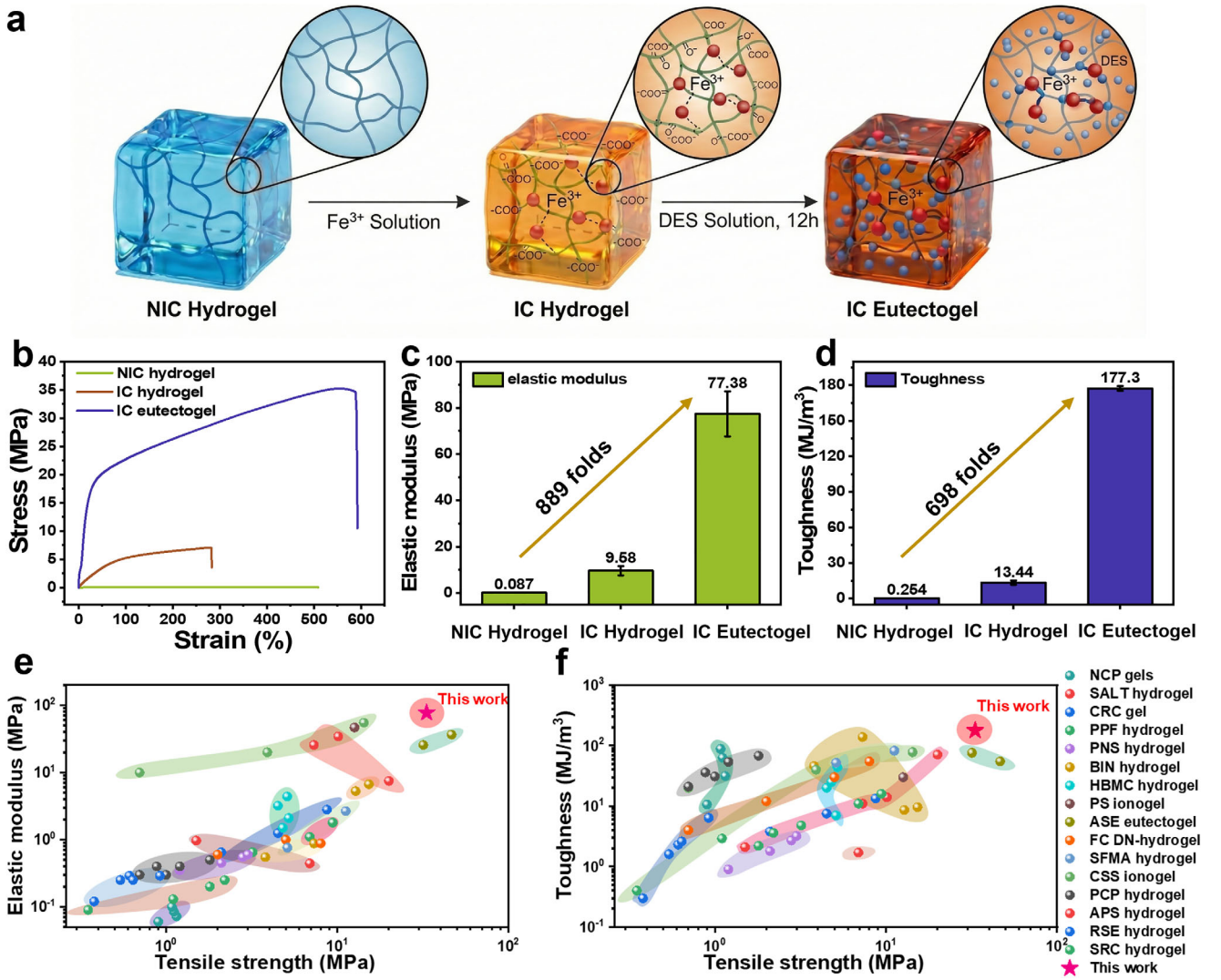

FIGURE 1 | Design strategy and mechanical evolution of the eutectogels. (a) Schematic illustration of the fabrication process. (b) Representative tensile stress–strain curves of the NIC Hydrogel, IC Hydrogel, and IC Eutectogel, revealing the dramatic enhancement in strength. (c) Comparison of elastic modulus and (d) toughness, highlighting an 889-fold increase in stiffness and a 698-fold increase in energy dissipation capability for the IC Eutectogel compared to the NIC precursor. Ashby plots comparing the (e) elastic modulus and (f) toughness against tensile strength for the IC Eutectogel (red star) versus various state-of-the-art gels reported in the literature.

The success of this sequential reinforcement strategy is quantitatively validated by the tensile stress–strain behaviors shown in Figure 1b, and the enlarged stress–strain curve of the NIC Hydrogel is shown in Figure S1. The pristine NIC Hydrogel behaves as a typical soft material, exhibiting negligible tensile strength (0.053 MPa) and elastic modulus (0.087 MPa), characteristic of a loosely cross-linked network. Upon the introduction of Fe^{3+} coordination, the IC Hydrogel shows a distinct improvement, with the tensile strength rising to 7.02 MPa and the modulus increasing to 9.58 MPa (Figure 1c). However, the most dramatic leap in performance occurs after the solvent exchange with DES. The IC Eutectogel exhibits an ultra-high tensile strength of 34.58 MPa, representing a nearly fivefold increase over the IC Hydrogel and a staggering ~650-fold increase over the NIC precursor.

This evolutionary leap is further highlighted by the statistical comparison of elastic modulus and toughness. As depicted in Figure 1c, the elastic modulus surges from 0.087 MPa (NIC) to 77.38 MPa (IC Eutectogel), corresponding to an 889-fold enhancement. Similarly, the toughness (Figure 1d), which represents the energy dissipation capability, increases from a trivial 0.254 MJ/m^3 to an unprecedented 177.3 MJ/m^3. This represents a 698-fold amplification in toughness. Such exceptional mechanical reinforcement is attributed to the synergistic effect of the high-density ionic coordination domains (induced by Fe^{3+}) and the strong hydrogen bonding network formed by the DES molecules, which collectively restrict chain slippage while allowing effective energy dissipation under large deformation.

To position our material within the broader context of soft matter research, we compared the mechanical performance of the IC Eutectogel with a wide range of advanced hydrogels, ionogels, and eutectogel reported in the literature [12, 24–38]. As illustrated in the plots of elastic modulus vs. tensile strength (Figure 1e, bottom left) and toughness vs. tensile strength (Figure 1f), our

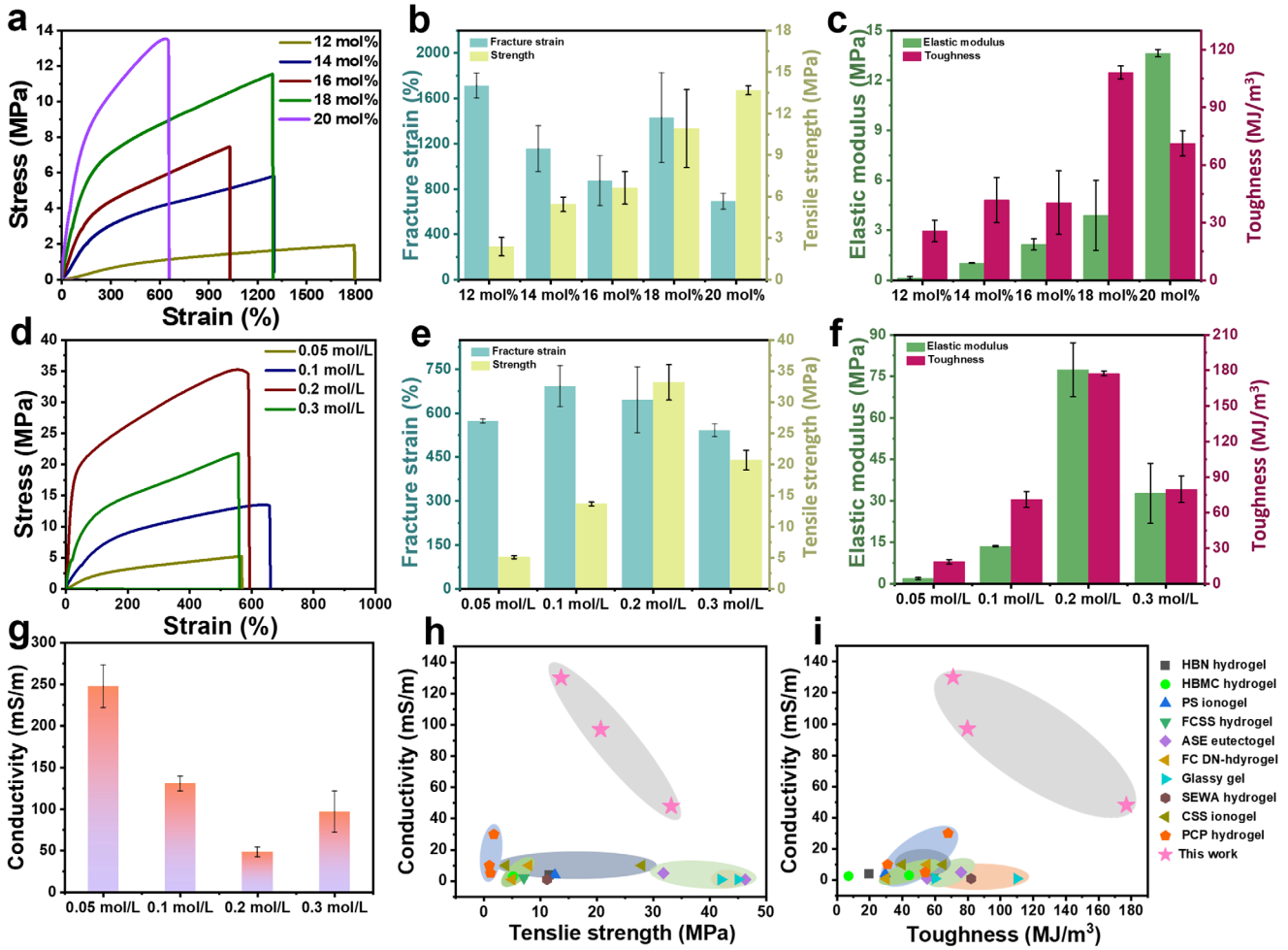

FIGURE 2 | Optimization of mechanical robustness and ionic conductivity. (a) Stress–strain curves, (b) statistical strength/strain, and (c) elastic modulus/toughness as a function of acrylic acid content. (d) Stress–strain curves, (e) statistical strength/strain, and (f) elastic modulus/toughness as a function of Fe^{3+} concentration. (g) Ionic conductivity of eutectogels with different iron concentrations. (h) ionic conductivity vs. tensile strength and (i) ionic conductivity vs. toughness, demonstrating that the optimized eutectogel (pink star) successfully decouples mechanical rigidity from ionic conductivity, occupying the superior top-right region.

work (marked by the red star) occupies the distinct top-right corner, signifying a superior combination of stiffness, strength, and toughness. Therefore, the resultant IC Eutectogel transcends the performance boundaries of traditional polymer networks, effectively bridging the gap between soft hydrogels and rigid engineering plastics.

2.2 | Optimization of Mechanical and Electrical Properties

To achieve the unprecedented synergy of characteristics as set out, we carried out a systematic two-stage optimization to adjust the cross-linking density and ionic interactions. The molar fraction of acrylic acid (AA) dictates the theoretical density of coordination sites along the polymer backbone. As shown in Figure 2a, increasing the AA content from 12 mol% to 20 mol% resulted in a marked transition from a compliant, highly stretchable network to a stiff, rigid matrix. Specifically, the tensile strength rose monotonically from ~1.8 to ~13.5 MPa, while the fracture strain decreased from 1712% to 691% (Figure 2b). This trend confirms that a higher density of carboxyl groups (-COOH) facilitates more extensive coordination with metal ions, restricting chain mobility. However, abnormal fracture strain was observed at a concentration of 18% mol. The anomalous peak in fracture strain is not an experimental error, but rather a compelling manifestation of the optimal topological spot within our dynamic supramolecular network. To definitively prove this mechanism and provide direct microstructural and dynamic evidence, we performed SAXS and rheological frequency sweeps on the 16 mol%, 18 mol%, and 20 mol% eutectogels, and the newly added results perfectly corroborate our hypothesis. As shown in Figure S2, the SAXS profiles reveal that the 18 mol% sample exhibits the highest scattering intensity in the low-q region compared to both the 16 mol% and 20 mol% samples. This confirms that at precisely 18 mol%, the Fe^{3+}-carboxylate ionic domains reach an optimal spatial distribution and maximal clustering density, forming the most robust sacrificial network without suffering from the extreme steric hindrance and structural homogenization that occurs in the over-cross-linked 20 mol% state.

Dynamically, this structural optimization translates into maximized energy dissipation, which is directly validated by our rheological measurements. As shown in Figure S3, in the low-to-medium frequency range, which corresponds to the time scale of our macroscopic quasi-static tensile tests, the loss factor (tan δ) of the 18 mol% sample rapidly climbs to a broad maximum of approximately 0.65, significantly outperforming the other groups. In contrast, the 16 mol% network lacks sufficient sacrificial bonds to dissipate energy (tan δ remains around 0.2), while the over-cross-linked 20 mol% network behaves more like a rigid elastic solid at low frequencies, severely restricting chain mobility and energy dissipation. Therefore, during large tensile deformations, the perfectly tuned dense ionic domains in the 18 mol% sample undergo massive, highly efficient reversible dissociation and chain friction. This maximized energy dissipation capability effectively homogenizes the internal stress and blunts the propagation of macroscopic cracks, thereby endowing the polymer chains with sufficient time and space to slide and extend, which fundamentally explains the anomalous and highly beneficial extension in ultimate fracture strain before the network inevitably turns brittle at higher concentrations.

Figure 2c shows that the elastic modulus and toughness increase with the content of AA. Notably, the sample with 18–20 mol% AA struck an ideal balance, providing a robust skeleton for subsequent ionic engineering while retaining sufficient extensibility. As the concentration of AA increases, the fracture strain of the gel further decreases. Figure S4 shows that for a gel with a concentration of 22 mol%, the elongation after fracture has decreased to approximately 450%.

To clarify the individual contributions of the Fe^{3+} coordination and the DES molecules, we systematically prepared two control groups for comparison, the eutectogel without Fe^{3+} (containing only the DES matrix without ionic coordination) and the hydrogel without DES (soaking in the 0.2 mol/L Fe^{3+} but without DES). As demonstrated in Figure S5, the sample without Fe^{3+} exhibits a high fracture strain of 817.7%, but extremely low tensile strength (0.88 MPa) and elastic modulus (0.38 MPa). This clearly defines the role of DES, it primarily acts as a plasticizing matrix that forms a ubiquitous, dynamic hydrogen-bonding network, which ensures exceptional stretchability but lacks sufficient strong nodes to bear heavy loads. Conversely, the sample without DES exhibits a tensile strength of 1.57 MPa and a modulus of 0.28 MPa with a strain of 572.3%. This reveals the role of Fe^{3+}, while it provides strong ionic coordination cross-linking to reinforce the network, the highly swollen nature of the aqueous environment keeps the polymer chains loose, preventing the realization of extreme strength. However, when both components are synergistically combined in the 0.2 mol/L eutectogel, the mechanical properties experience an exponential leap, achieving a tensile strength of 34.58 MPa, an elastic modulus of 77.38 MPa, and a toughness of 177.3 MJ/m^3. This stark contrast perfectly illustrates their synergistic mechanism. The Fe^{3+} ions serve as the rigid, load-bearing coordination nodes (the skeleton) to withstand high external stress. Concurrently, the introduction of DES replaces water molecules, driving a massive volume shrinkage and densification of the polymer network. This dense DES environment not only geometrically amplifies the effective cross-linking density of the Fe^{3+} domains but also dissipates enormous amounts of energy through hydrogen bond rupture and solvent friction during large deformations, thereby preventing brittle fractures.

Based on the optimized polymer matrix, we further modulated the cross-linking degree by varying the Fe^{3+} concentration from 0.05 to 0.3 mol/L. This step proved critical in defining the final performance. As shown in Figure 2d–f, at low concentrations (0.05–0.1 mol/L), the network exhibited relatively low strength (<15 MPa) and modulus, indicating an under-cross-linked state where the sparse ionic domains were insufficient to sustain high loads. At the optimal concentration (0.2 mol/L), the mechanical properties reached a spectacular peak. The tensile strength surged to 34.58 MPa, accompanied by an elastic modulus of 77.38 MPa and a volumetric toughness of 177.3 MJ/m^3. This suggests the formation of a critical percolation network of high-density ionic domains, which effectively maximizes the energy dissipation via bond rupture and reconstruction. However, at high concentrations (0.3 mol/L), a "turnover" effect was observed, where the strength dropped to ~22 MPa and the strain decreased significantly. This decline is attributed to "over-cross-linking," which creates excessive steric hindrance and network heterogeneity, causing premature brittle fracture before the self-strengthening mechanism can be fully activated.

While densification enhances strength, it inevitably impacts ion transport. Figure 2g reveals that the ionic conductivity decreases as the Fe^{3+} concentration increases from 0.05 mol/L (~250 mS/m) to 0.2 mol/L (~50 mS/m). This reduction occurs because the formation of dense ionic domains restricts the mobility of free ions and tortuous migration pathways. However, even at the mechanically optimal condition (0.2 mol/L), the eutectogel retains a conductivity of ~50 mS/m, which is more than sufficient for sensing applications. Interestingly, at 0.3 mol/L, a slight recovery in conductivity was observed, potentially due to the presence of uncoordinated excess ions or phase separation, further confirming that 0.2 mol/L is the optimal saturation point.

To highlight the significance of this work, we mapped the properties of our optimized IC Eutectogel against a comprehensive library of high-performance hydrogels, ionogels, and eutectogel reported in the literature [16, 23, 29–35, 39]. As illustrated in the Ashby plots of conductivity vs. tensile strength (Figure 2h) and conductivity vs. toughness (Figure 2i), most existing materials fall into the grey/colored ovals, suffering from the classic trade-off, high strength/toughness typically comes at the expense of low conductivity (such as glassy gels), while highly conductive gels are often mechanically weak. Our work (marked by the pink stars) uniquely occupies the top-right quadrant of these charts. This positioning signifies a successful decoupling of ionic conductivity from structural rigidity, establishing a new material paradigm that simultaneously offers extreme mechanical robustness (34.58 MPa, 177.3 MJ/m^3) and functional conductivity, outperforming state-of-the-art counterparts.

2.3 | Structural Evolution and Microscopic Mechanism

To elucidate the microscopic origins of the optimization in mechanical properties, specifically why the 0.2 mol/L Fe^{3+} concentration yields the peak performance, we conducted a

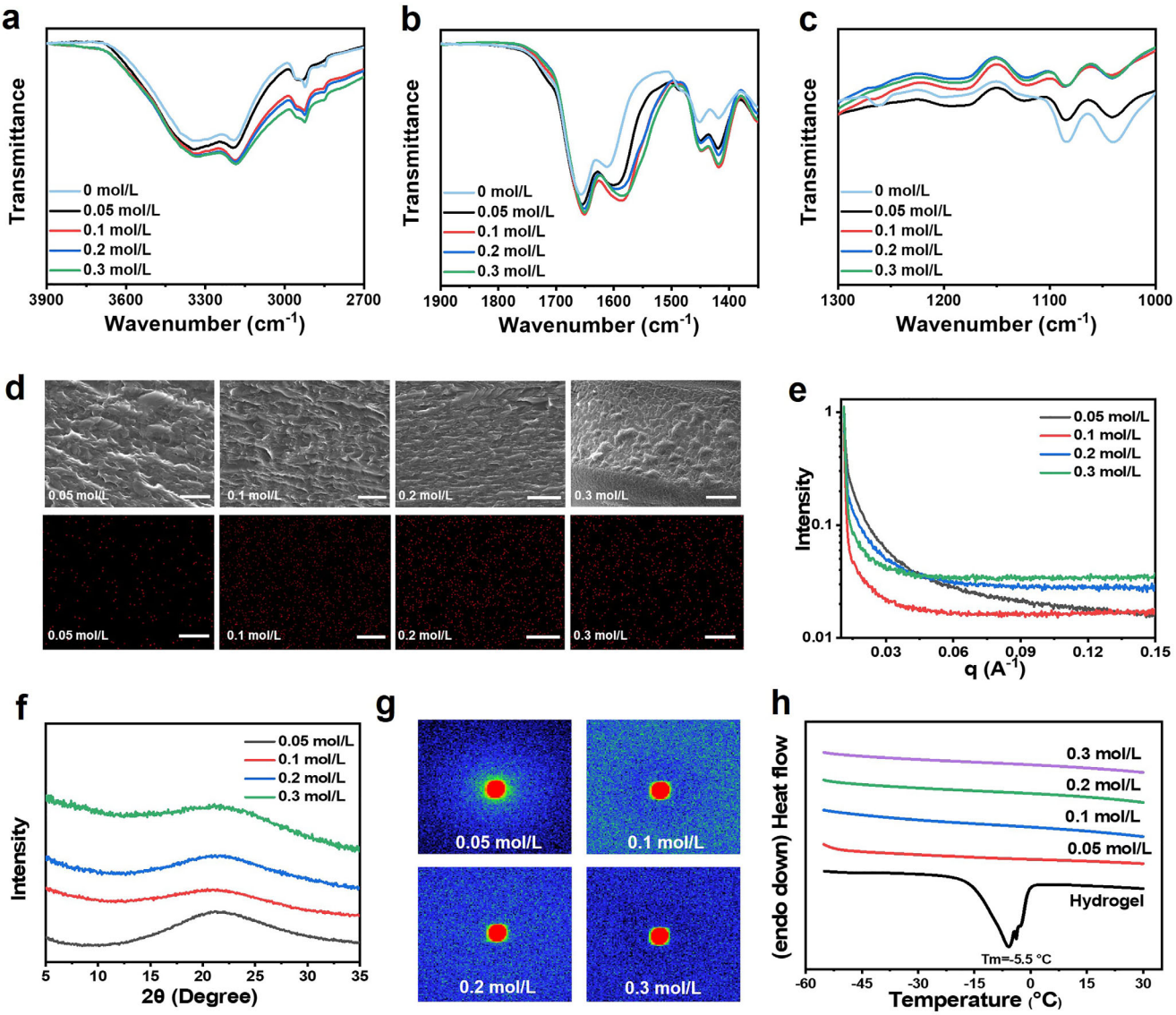

FIGURE 3 | Structural characterization and microscopic reinforcing mechanism. FTIR spectra of eutectogels with varying Fe^{3+} concentrations in the regions of (a) O—H/N—H stretching, (b) C═O stretching, and (c) fingerprint region. (d) SEM images (top) and corresponding EDS elemental mapping of Iron (bottom). (e) 1D SAXS profiles showing the low q upturn. (f) 1D WAXS profiles confirming the fully amorphous nature of the polymer network (absence of crystalline peaks). (g) 2D SAXS patterns exhibiting isotropic scattering rings. (h) DSC thermograms verifying the anti-freezing capability of the eutectogels down to −50°C compared to the water-based hydrogel.

comprehensive structural analysis ranging from molecular interactions to nano-scale morphology. The evolution of chemical bonding with varying Fe^{3+} concentrations was traced using FTIR spectroscopy [40, 41]. As shown in Figure 3a, the high-frequency region is dominated by the stretching vibrations of hydroxyl (-OH) and amine (-NH) groups, which act as sensitive probes for the hydrogen bonding environment within the DES-polymer matrix. All samples exhibit a broad, intense absorption band centered around 3300–3350 cm^{-1}. This band originates from the overlapping O—H stretching of the DES (ethylene glycol and choline chloride) and the N—H stretching of the polyacrylamide backbone. As the Fe^{3+} concentration increases from 0.05 to 0.2 mol/L, this peak exhibits a noticeable redshift and an increase in relative intensity, and redshift in FTIR typically indicates a strengthening of intermolecular interactions. In this context, the high-valence metal ions Fe^{3+} act as strong Lewis acids, which polarize the surrounding solvent and polymer molecules. This "salting-out" like effect compresses the solvation shell and promotes more extensive and stronger hydrogen bonding between the DES molecules and the polymer chains. This enhanced H-bond network serves as the first line of defense for energy dissipation. The most critical changes occur in the carboxylate vibration regions. Figure 3b provides the most direct evidence for the Fe^{3+}-carboxylate coordination, which acts as the skeleton of the eutectogel's strength. The peak at approximately 1650 cm^{-1}, attributed to the C═O stretching of the acrylamide unit, remains relatively stable but sharpens. The distinct peak shifts relative to the blank sample provide direct evidence for the successful formation of Fe^{3+}-COO^{-} coordination bonds. This also suggests that the acrylamide segments provide a stable backbone but are less involved in direct metal coordination compared to the acrylic acid units. The most critical evolution

occurs in the carboxylate (-COO^-) vibration region from 1550–1400 cm^{-1}. In the low-concentration sample (0.05 mol/L), the peaks are relatively broad and weak. As the concentration rises to 0.1 and 0.2 mol/L, two distinct bands emerge and intensify, the asymmetric stretching vibration, at roughly 1540–1560 cm^{-1} and the symmetric stretching vibration at 1400–1420 cm^{-1}. The appearance of these specific bands confirms the deprotonation of carboxylic acid groups (-COOH) and the formation of stable Fe^{3+}-carboxylate coordination complexes. As shown in Figure 3c, the fingerprint region further elucidates the interaction between the solvent and the polymer skeleton. The peaks in the 1000–1100 cm^{-1} range (associated with C—O stretching of EG and C—N stretching) show a clear intensity increase from 0 to 0.1 mol/L. The 0 mol/L sample represents a loose, highly swollen network where the DES molecules possess high degrees of freedom, resulting in distinctly different, relatively sharp characteristic peaks. The introduction of even a minimal amount of Fe^{3+} (0.05 mol/L) initiates strong coordination and the salting-out effect, which triggers macroscopic volume shrinkage and forces the previously free DES molecules into a restricted, tightly hydrogen-bonded environment, causing an immediate and dramatic spectral shift and peak broadening compared to the blank group. As the concentration increases from 0.05 to 0.1 mol/L, the network undergoes its most drastic phase of densification, squeezing the DES molecules into tighter continuous channels and further altering their conformational environment, which explains the significant spectral changes in this specific range. However, as the Fe^{3+} concentration further increases from 0.1 to 0.3 mol/L, the global spatial confinement and the volume shrinkage of the polymer matrix reach a relatively stable thermodynamic plateau. The background DES matrix becomes structurally locked in its highly restricted state. Consequently, while additional Fe^{3+} continues to increase the density of localized carboxylate coordination sites on the polymer chains, the overall hydrogen-bonding environment and spatial conformation of the DES molecules remain saturated and stable. This spectroscopic "saturation point" perfectly corroborates the mechanical data in Figure 2d, explaining why the strength peaks at 0.2 mol/L and plateaus or drops thereafter.

The impact of coordination on the mesoscopic microstructure is visualized in the SEM images (Figure 3d). The sample with low iron content (0.05 mol/L) exhibits a relatively rough and textured surface, indicative of a loose network with lower cross-linking density. As the concentration increases to 0.2 mol/L, the surface transforms into a highly compact, smooth, and dense morphology. This confirms that the strong electrostatic attraction and coordination interactions have effectively collapsed the polymer chains into a tight network, which is the structural basis for the high tensile strength (34.58 MPa). At 0.3 mol/L, the surface appears excessively dense with some irregular features, hinting at potential heterogeneous aggregation. The corresponding EDS mapping shows that even at high concentrations, the Fe signals (red dots) remain uniformly distributed without macroscopic phase separation. This uniformity is crucial for ensuring consistent mechanical transmission and preventing stress concentration points. We also performed cryogenic scanning electron microscopy (Cryo-SEM) on the 0.05 and 0.2 M samples across multiple magnifications. The newly obtained hierarchical Cryo-SEM images provide clear and direct evidence effectively ruling out heterogeneous aggregation. As shown in Figure S6a, the multi-scale observation of the 0.05 M eutectogel reveals a relatively flat, continuous matrix interspersed with sparsely distributed, isolated micro-pores and localized micro-defects visible at higher magnifications. This morphology accurately reflects a loosely cross-linked and highly solvated state, where the low density of iron ions is insufficient to drive the global assembly of the polymer chains into a mature interconnected mesh. Crucially, when the Fe^{3+} concentration is increased to the mechanically optimal 0.2 M, as shown in Figure S6b, the network undergoes a profound morphological transition but does not show any macroscopic clumps, precipitates, or irregular phase-separated domains even under 20 000x magnification. Instead, the magnified views explicitly display a remarkably uniform, highly interconnected, and densely packed 3D nanofibrillar mesh. This homogeneous porous architecture confirms that the abundant Fe^{3+}-carboxylate coordination interactions act as evenly distributed cross-linking nodes throughout the entire matrix, successfully driving the uniform global densification of the polymer chains to form a perfect percolated network.

To bridge the gap between molecular interactions and macroscopic mechanics, we employed Small-Angle and Wide-Angle X-ray Scattering (SAXS/WAXS) to probe the mesoscopic structural evolution and the formation of ionic domains [42]. The 1D SAXS profiles (Figure 3e) and the corresponding 2D scattering patterns (Figure 3g) provide compelling evidence for the transition from a homogeneous network to a micro-phase separated structure driven by metal ion concentration. The scattering profile for the low-concentration sample (0.05 mol/L) is relatively flat and featureless in the low q region ($q < 0.05$ $Å^{-1}$), and its 2D pattern is diffuse and dark. This indicates a homogeneous distribution of polymer chains and isolated ionic pairs. At this stage, the ionic density is insufficient to trigger aggregation, resulting in a network that lacks strong reinforcement centers, correlating with its low mechanical strength (~4 MPa). A dramatic structural transition occurs at 0.1 mol/L and stabilizes at 0.2 mol/L. A distinct "upturn" in scattering intensity is observed in the low q region ($q < 0.03$ $Å^{-1}$), arising from the electron density contrast between the polymer matrix and the heavy-metal-rich regions. It signifies the aggregation of dispersed Fe^{3+}-carboxylate complexes into discrete nano-scale ionic domains. The intensity leap from 0.05 to 0.2 mol/L confirms that 0.2 mol/L represents a critical threshold. At this concentration, the ionic multiples are no longer isolated, they coalesce to form high-density, interconnected ionic domains that serve as "super-cross-links." These domains are robust enough to restrict chain slippage yet dynamic enough to dissipate energy. We also extracted the quantitative average radius of gyration (R_g) for the ionic domains. As shown in Figure S7, the progressive increase in R_g from 6.1 nm to approximately 8.7 nm provides direct mathematical evidence that with the optimization of the system, the initially smaller coordination nodes gradually grow and densify into highly robust, nano-scale ionic clusters. Crucially, the stabilization of the R_g value around 8.5 to 8.7 nm at optimal conditions perfectly explains why the network achieves maximal mechanical energy dissipation without undergoing detrimental macroscopic phase separation, which flawlessly corroborates our Cryo-SEM observations where the matrix remains highly homogeneous. These 6–9 nm dimensions perfectly match the spatial and topological requirements for efficient multi-chain sacrificial cross-linking nodes, thereby establishing a rigorous, quantitative

structure-property relationship bridging the nanoscale ionic rearrangement and the macroscopic mechanical leap.

We conducted comparative rheological amplitude sweep measurements on both the 0.2 and 0.3 mol/L eutectogels to quantitatively evaluate their dynamic yielding behaviors under increasing deformation. Figure S8 reveals a distinct, albeit moderate, shift in the structural yield point, defined as the crossover of the storage modulus and loss modulus. Specifically, the critical yield strain decreases from approximately 27% for the highly robust 0.2 mol/L sample to about 18% for the 0.3 mol/L sample. This moderate dynamic difference perfectly aligns with our macroscopic tensile results and physically explains why the mechanical properties experience a slight degradation rather than a continued increase or a catastrophic failure at 0.3 mol/L. In the 0.2 mol/L system, the dense and uniform ionic domains effectively distribute stress, requiring a higher critical strain to induce network yielding. In contrast, in the 0.3 mol/L system, while the primary polymer network remains largely robust, the newly formed loose clusters of excessive Fe^{3+} do not effectively participate in load bearing. Instead, they act as mild localized structural discontinuities. Under external deformation, these loose aggregates cannot efficiently transfer load or dissipate through reversible sacrificial bond rupture like the dense cores do. Consequently, they act as localized weak points that cause the overall network to yield at a slightly lower critical strain. Therefore, these loose clusters essentially hinder the materials from maintaining their optimal stress-transfer efficiency, fundamentally explaining the moderate decrease in macroscopic mechanical strength.

The WAXS curves (Figure 3f) for all samples exhibit only broad amorphous halos centered at 2θ about 20 to 25°, with no sharp crystalline peaks. This proves that the extraordinary strength of the eutectogel does not stem from polymer crystallization (which would reduce stretchability) but rather from the dense ionic cross-linking. It proves that the "ionic domains" detected by SAXS are amorphous aggregates rather than crystalline precipitates. 1D WAXS intensity profiles plotted against the scattering vector q (Figure S9), revealing the amorphous nature of the network with a characteristic halo at approximately 1.5 $Å^{-1}$. According to Bragg's law, this corresponds to an average interchain or intermolecular spacing of 4.2 Å, which is characteristic of the disordered packing of amorphous polymer chains and DES molecules. Combining SAXS and WAXS, we conclude that the extraordinary mechanical properties of the 0.2 mol/L eutectogel originate from a unique microstructure, that is the amorphous polymer matrix reinforced by a percolated network of high-density, non-crystalline ionic domains. These domains act as sacrificial bonds that are strong enough to provide high stiffness (77.38 MPa) but disordered enough to allow reversible deformation.

Finally, the thermal stability conferred by the DES was verified by DSC (Figure 3h). The control hydrogel exhibits a sharp endothermic peak at −5.5°C, corresponding to the melting of ice crystals. In stark contrast, all eutectogel samples (0.05 to 0.3 mol/L) show flat thermal curves with no crystallization or melting peaks throughout the cooling and heating cycles down to −50°C. This result confirms that the hydrogen bond acceptors/donors in the DES have formed a stable complex with the polymer chains, effectively disrupting the formation of the ice lattice. This ensures that the structural integrity and ionic conductivity discussed above are preserved even in sub-zero environments.

2.4 | Dynamic Mechanical Adaptability

Beyond static robustness, the dynamic reversibility of the ionic domains endows the eutectogel with exceptional fatigue resistance and a unique self-strengthening capability. As shown in Figure 4a, the energy dissipation mechanism was first evaluated via cyclic loading–unloading tests at 100% strain, where the extensive hysteresis loop in the first cycle indicates significant energy dissipation attributed to the rupture of sacrificial ionic bonds and the friction of polymer chains. Although peak stress decreases noticeably during the first few cycles due to the Mullins effect, representing the alignment of chains and the dissociation of weak cross-links, the maximum stress and the hysteresis loop area stabilize and remain almost constant for over 200 cycles after the initial training phase (Figure 4b). This stable fatigue resistance confirms that the primary polymer backbone remains intact while the ionic cross-links undergo reversible dissociation and association to sustain the load. As shown in Figure S10, the stress ratio of the 200th cycle was 51.3%. To probe the kinetics of network reconstruction and its dependence on ionic density, interrupted cyclic tests with varying resting times were conducted on eutectogels with four different iron ion concentrations (Figure 4c–f). In this protocol, each sample was first subjected to a 100% strain loading–unloading cycle, followed by resting intervals of 1, 5, and 30 min before re-stretching. Figure S11 shows the cyclic curve after waiting for 60 min. As shown in Figure 4c and Figure S12, this sample exhibits the most pronounced "self-strengthening" phenomenon. After a short rest of 1 min, the stress recovers significantly but remains below the pristine curve. However, as the resting time extends to 30 min, a dramatic transformation occurs, the re-loading curve not only fully recovers but distinctively surpasses the original path, exhibiting a higher modulus and peak stress, the recovery efficiency reaches 98.9% and after 60 min, the value increases to 152.9%. This implies that in a loosely cross-linked network, the abundant uncoordinated ligands allow the ions to migrate freely and capture new sites, effectively "upgrading" the network topology during rest. As the Fe^{3+} concentration increases, the transitional behavior is observed. For the 0.1 and 0.2 M samples (Figure 4d,e and Figures S13 and S14), the 30-min recovery curve still exceeds the original, and the recovery efficiency reaches 103.9% and 119.9%. At the highest concentration, the network exhibits the saturation effect (Figure 4f and Figure S15). Even after 30 min of rest, the re-loading curve closely traces the original path without any overshoot. The high density of existing cross-links likely creates significant steric hindrance and reduces the number of free carboxyl sites available for new coordination, thereby limiting the potential for further structural optimization, the recovery efficiency decreases to 103.5%.

To further verify the distinct concentration-dependent reconstruction mechanisms proposed above, we performed time-resolved cyclic tensile tests on the 0.05 and 0.3 M eutectogels. In these experiments, the samples were subjected to repeated loading–unloading cycles with a fixed 30-min resting interval between each cycle to allow for structural evolution. As shown

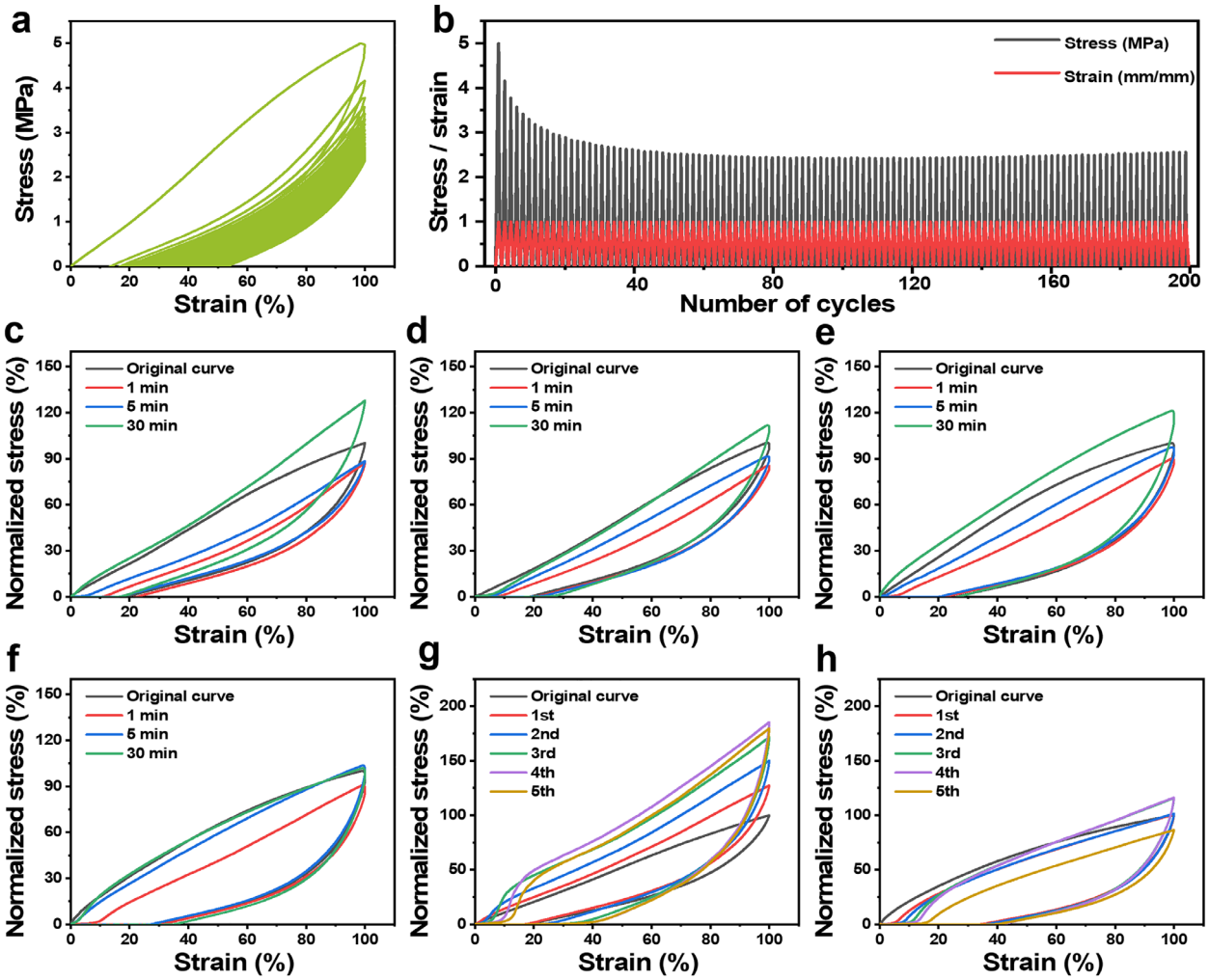

FIGURE 4 | Dynamic mechanical adaptability and "muscle-like" self-strengthening behavior. (a) Cyclic loading–unloading curves of the optimized eutectogel at 100% strain. (b) Stress and strain of gel for 200 cycles, showing stable energy dissipation after initial training. Normalized stress–strain curves of interrupted cyclic tests with varying resting times (1, 5, 30 min) for eutectogels with Fe^{3+} concentrations of (c) 0.05 M, (d) 0.1 M, (e) 0.2 M, and (f) 0.3 M. Time-resolved cyclic strengthening tests with 30-min intervals for (g) 0.05 M and (h) 0.3 M samples.

in Figure 4g and Figure S16, the 0.05 M sample exhibits a rapid and robust self-strengthening response. Notably, a distinct stress overshoot is observed immediately from the first re-stretching cycle (1st cycle), indicating that the abundant uncoordinated carboxyl sites facilitate rapid ionic rearrangement even after a single deformation event. The peak stress continues to rise progressively, reaching a maximum of 185% of the initial value around the 4th cycle. This suggests that repeated stretching aligns the polymer chains, progressively exposing more binding sites for the mobile iron ions to lock into, thereby incrementally increasing the cross-linking density. By the 5th cycle, a slight decrease in peak stress is observed compared to the 4th cycle, likely due to the accumulation of irreversible chain scission beginning to counteract the ionic healing. However, crucially, the stress level at the 5th cycle remains significantly higher than the initial state, proving that the constructive ionic rearrangement dominates over the destructive fatigue process in this loosely cross-linked network. In sharp contrast, the 0.3 M sample displays a trajectory dominated by saturation and fatigue. As shown in Figure 4h and Figure S17, for the first three cycles, the re-loading curves almost perfectly overlap with the initial curve. This lack of strengthening confirms the saturation hypothesis, that is the high density of existing cross-links and the scarcity of free coordination sites create significant steric hindrance, effectively locking the network and preventing the mobile ions from forming new, stronger domains during the rest period. A marginal stress increase is observed only at the 4th cycle, the stress ratio reaches 115.1%, possibly due to minor local reordering. However, by the 5th cycle, the stress drops precipitously to a level lower than the initial cycle, the stress ratio decreases to 86.1%. This indicates that in such a rigid, over-saturated network, the mechanism of cumulative mechanical damage (bond rupture and crack propagation) overwhelms the negligible self-recovering capability. Unlike the 0.05 M sample, the 0.3 M gel lacks the "dynamic freedom" to repair the structural defects caused by cyclic loading, leading to a net degradation in performance. Although the abundant free Fe^{3+} ions in the 0.3 mol/L system possess high mobility and are expected to participate in rapid dynamic dissociation and migration during deformation, the macroscopic self-strengthening effect of the eutectogel depends not only on the kinetic mobility of the ions but, more importantly, on their ability to successfully reconstruct an effective,

load-bearing cross-linked network along the polymer backbone. In the 0.2 mol/L system, the dynamically dissociated Fe^{3+} ions can efficiently find and coordinate with available carboxylate sites during stretching, forming a highly oriented and strengthened topology. In contrast, in the over-dosed 0.3 mol/L system, the effective coordination sites on the polymer chains are almost saturated. Consequently, even though the free Fe^{3+} ions and loose clusters can move rapidly under stress, they cannot find sufficient available anchoring sites on the polymer backbone to reconstruct new effective stress-transferring nodes.

We also have measured the baseline ionic conductivity of 0.05 and 0.3 M eutectogels before and after the 5-cycle self-strengthening process. Interestingly, the experimental results show that the ionic conductivity did not decrease; instead, it anomalously increased by 1.62 ± 0.09 and 1.90 ± 0.38 times, respectively. This phenomenon can be well explained by the fact that macroscopic ionic conductivity is determined synergistically by the concentration of available charge carriers and the geometric dimensions of the ion transport channels. Regarding the charge carriers, although the stress-triggered rearrangement does consume a certain amount of free Fe^{3+} ions to form stronger cross-linking domains, these transition metal ions constitute only a minor fraction of the total conductive species. The primary charge carriers in our system are the massive amounts of highly mobile choline cations and DES, which remain virtually unaffected by the polymer-metal coordination process. More importantly, regarding the transport channels, the cyclic mechanical stretching inevitably induces a local orientation of the polymer chains along the stretching direction. This stress-induced orientation significantly reduces the 3D tortuosity of the polymer network, effectively straightening the internal ion transport pathways. Consequently, the high-mobility DES ions can shuttle through these geometrically optimized, less obstructed, and highly oriented continuous phases with substantially lower transport resistance. The combination of sustained abundant DES carriers and structurally optimized, low-tortuosity pathways ultimately leads to the significant multiplication of the macroscopic conductivity after mechanical training.

To validate the proposed stress-triggered ionic rearrangement mechanism, we have supplemented our study with comprehensive microscopic characterizations. First, to visualize the structural evolution, we performed polarized optical microscopy (POM) on the optimal eutectogel. As shown in Figure S18, the profound optical transition from an initially dark, optically isotropic field to pronounced macroscopic birefringence after five tensile cycles visually confirms that cyclic stress effectively forces the randomly distributed polymer chains and ionic domains to dynamically dissociate, align, and reconstruct into a highly ordered anisotropic topology along the loading direction.

To further provide quantitative spectroscopic and morphological proof of this dynamic reconstruction at the molecular level, we performed comparative FTIR and SAXS analyses on the samples before and after the 5th cycle. To build rigorous and comprehensive proof, we evaluated both the highly self-strengthening 0.05 mol/L sample and the over-cross-linked 0.3 mol/L sample as a negative control. For the 0.05 mol/L eutectogel, which macroscopically exhibits a remarkable peak stress enhancement up to 185%, the microscopic data mirror this constructive evolution correspondingly. As shown in Figure S19a, there is a noticeable redshift of the characteristic peak from 1658 to 1655 cm^{-1}, accompanied by an obvious increase in the intensity of the carboxylate coordination peaks after 5 cycles. This redshift and intensification indicate a strengthening of intermolecular interactions, specifically demonstrating that during deformation and resting, previously uncoordinated carboxyl groups are exposed and captured by mobile free iron ions to form new and stronger Fe^{3+}-carboxylate coordination complexes. Concurrently, the SAXS profile of this 0.05 mol/L sample (Figure S19b) shows a substantial increase in scattering intensity in the low-q region ($q < 0.03$ $Å^{-1}$) after 5 cycles. This provides direct morphological evidence that the newly formed coordination bonds drive the dispersed ions to aggregate in situ, resulting in the densification and growth of robust amorphous ionic domains.

Conversely, the data from the 0.3 mol/L sample provides a compelling and nuanced perspective on why abundant free ions do not guarantee macroscopic strengthening in an over-cross-linked network. Macroscopically, this sample exhibits a stress drop to 86.1% by the 5th cycle. However, the updated FTIR spectra (Figure S20a) still show a redshift from 1654 to 1652 cm^{-1} and an increase in the carboxylate coordination peak intensity (lower transmittance). This intriguing observation indicates that stress-triggered ionic rearrangement indeed occurs due to the high kinetic mobility of free Fe^{3+}, but it manifests as a forced, destructive shift in the state of coordination. Due to the excess of iron ions relative to the available carboxylate groups in this saturated system, the cyclic stretching disrupts the initial strong, highly coordinated ionic clusters. During the resting phase, the high steric hindrance and disrupted topology force the iron ions to re-coordinate in lower coordination states. For instance, a strong cross-linking center where one Fe^{3+} coordinates with multiple carboxylate groups from different chains may be reorganized into weaker, lower-valency interactions. While the absolute number of localized metal–ligand interactions increases (reflecting in the stronger FTIR absorbance), the overall networking efficiency and cross-link strength are fundamentally weakened, leading to macroscopic fatigue. This hypothesis is flawlessly corroborated by its SAXS profile (Figure S20b), which exhibits a distinct decrease in the low-q scattering intensity after training. The transition from high-coordination cross-linking centers to numerous low-coordination interactions essentially leads to the fragmentation of the previously large and dense ionic domains. The smaller, less densely packed loose ionic clusters scatter less prominently in the low-q region. By combining the visual macroscopic alignment from POM with the direct correlation between mechanical performance and the densification versus fragmentation of ionic domains from FTIR and SAXS, we believe we have definitively validated the stress-triggered ionic rearrangement mechanism and perfectly resolved the structural paradox of the 0.3 mol/L system.

2.5 | Application as Ultrasensitive Strain Sensors

To demonstrate the practical utility of the optimal eutectogel in wearable electronics, a resistive strain sensor was fabricated by assembling the gel with copper wire interconnects, as

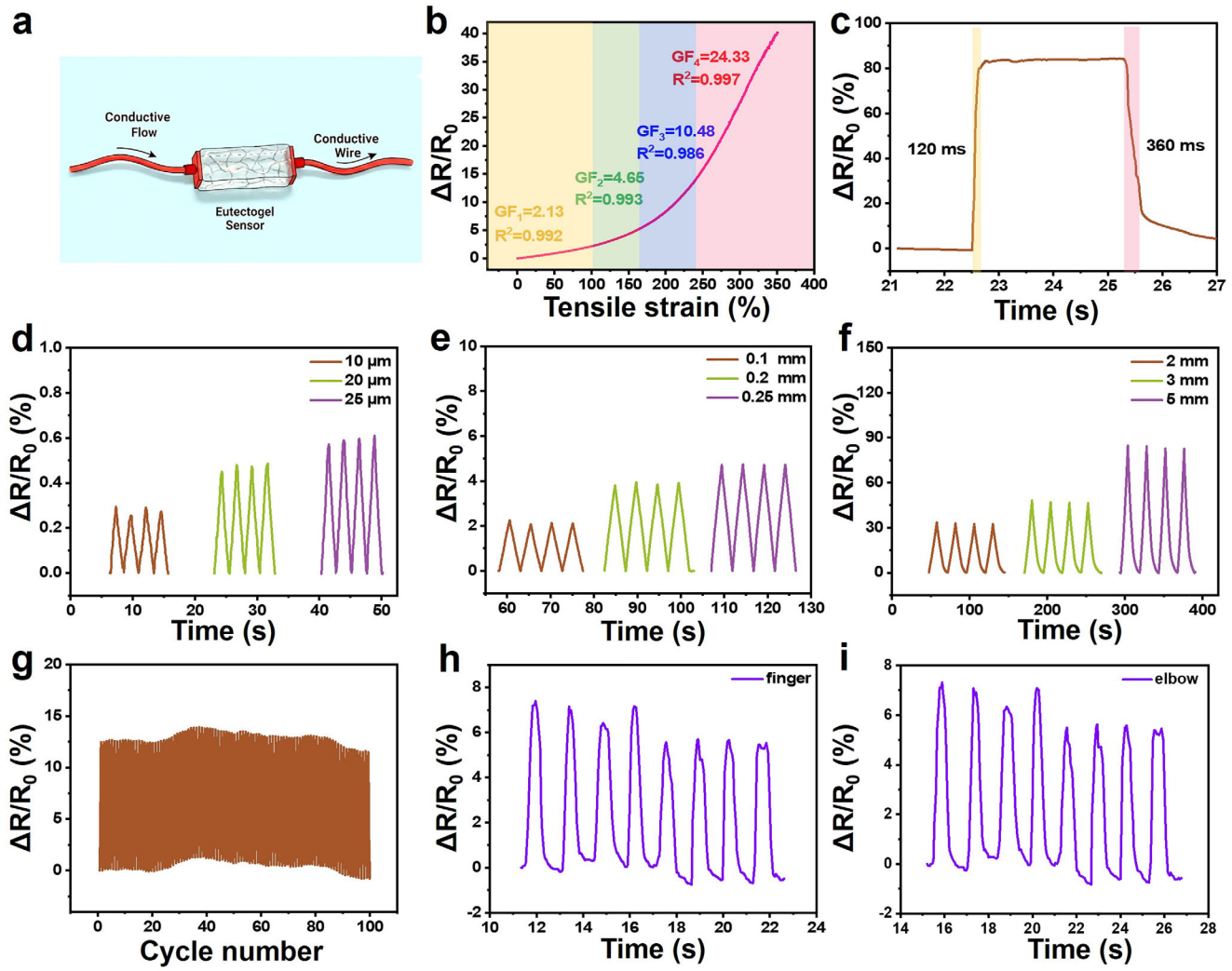

FIGURE 5 | Applications for the resistive strain sensor. (a) Schematic diagram of the resistive sensor assembly. (b) Relative resistance changes versus tensile strain. (c) Fast response and recovery times. (d) Detection of ultra-small micro-displacements (10, 20, and 25 μm), highlighting the low detection limit. Stable sensing performance under (e) small strains (0.1–0.25 mm) and (f) medium strains (2–5 mm). (g) Cyclic durability test over 100 cycles. Real-time monitoring of human motions such as (h) finger bending and (i) elbow flexion.

illustrated in Figure 5a. The electro-mechanical sensitivity was systematically evaluated by monitoring the relative resistance change ($\Delta R/R_0$) under varying tensile strains. To confirm the biocompatibility of these gels, we have supplemented an in vitro cytotoxicity assay using the standard Cell Counting Kit-8 (CCK-8) method. For this assay, we specifically selected Human Dermal Fibroblasts (HDF) as the model cell line. Since HDFs are the primary structural cells residing in the human dermis. As shown in Figure S21, the eutectogels exhibited outstanding biocompatibility. After 24 h of incubation, the cell viabilities for the four concentrations were remarkably high, recorded at 103.6%, 100.5%, 102.9%, and 99.2%, respectively. Even after extending the incubation period to 48 h, the cell viabilities remained highly robust at 96.8%, 94.9%, 90.2%, and 90.4%. Our results, remaining entirely above 90% even after 48 h for all sample groups, definitively demonstrate that the chosen deep eutectic solvent is highly benign at the cellular level. Therefore, these quantitative cytotoxicity results conclusively prove that our eutectogels are exceptionally safe for direct epidermal attachment in real-time physiological monitoring.

We further test the sensing properties of these gel-based sensors, as shown in Figure 5b, the sensor exhibits a positive behavior where the resistance increases monotonically with strain. Interestingly, the sensitivity curve is non-linear and can be divided into four distinct stages, revealing a "strain-activated" sensing mechanism. In the initial low-strain region (0%–100%), the gauge factor (GF) is 2.13, which is primarily governed by the geometric deformation of the gel geometry. However, as the strain increases, the GF rises progressively to 4.65 (100%–170%) and 10.48 (170%–240%), eventually reaching a remarkable peak value of 24.33 in the high-strain region (240%–350%). This exponential increase in sensitivity at large deformations is attributed to the synergistic effect of geometric elongation and the intrinsic microstructural evolution, where the rapid disconnection of ionic conductive pathways and the reversible widening of the ionic domains under high tension significantly amplify the resistance change. We also conduct a comprehensive literature survey focusing on recently reported gel-based strain sensors, including hydrogels, ionogels, and eutectogels over the past two years. As clearly demonstrated in Figure S22, most conventional gel-based sensors

typically exhibit GF values strictly below 15. Furthermore, those sensors that do achieve relatively higher sensitivities almost universally suffer from severe mechanical trade-offs, with their tensile strengths confined to the low-MPa or even sub-MPa range. In stark contrast, our designed eutectogel uniquely occupies the superior top-right corner of the chart. The unprecedented convergence of an ultra-high GF of 24.33 and an extreme tensile strength of 34.58 MPa represents a significant breakthrough, surpassing the typical performance boundaries observed in current flexible electronics.

Beyond high sensitivity, the sensor demonstrates exceptional resolution and response speed. Figure 5c reveals that the sensor possesses a rapid response time of approximately 120 ms and a recovery time of 360 ms, ensuring real-time signal acquisition without significant hysteresis. Crucially, the sensor can detect extremely minute deformations. As evidenced in Figure 5d, clear and distinguishable signal waves were recorded even under micro-displacements of 10, 20, and 25 μm, the corresponding strain was 0.1%, 0.2%, and 0.25%, respectively. This ultra-low detection limit allows the sensor to capture subtle physiological signals that are often missed by conventional hydrogel sensors. Furthermore, the sensor maintains stable signal outputs across a broad range of small strains (0.1–0.25 mm, Figure 5e) and medium strains (2–5 mm, Figure 5f), exhibiting excellent linearity and repeatability in these regimes. The long-term reliability was further verified by a cyclic durability test (Figure 5g), where the resistance variations remained consistent and stable over 100 continuous loading–unloading cycles, confirming the structural integrity of the eutectogel network against fatigue. Leveraging these superior properties, the resistive sensor was mounted on a volunteer's body to monitor human motions. For small-scale joint movements, such as finger bending (Figure 5h), the sensor produced sharp, repeatable waveforms that corresponded perfectly with the bending angles. Similarly, for the movements like elbow flexion (Figure 5i), the sensor exhibited a larger response amplitude while maintaining signal stability. These results collectively demonstrate that the eutectogel-based resistive sensor combines an ultra-wide working range, high sensitivity (GF up to 24.33), and high precision (10 μm limit), making it an ideal candidate for comprehensive human–machine interface applications.

To further expand the application scope into compressive stress monitoring, the eutectogel was assembled into a capacitive pressure sensor by sandwiching the dielectric gel layer between two copper electrodes, as depicted in Figure 6a. The sensing performance was quantitatively evaluated by measuring the relative capacitance change ($\Delta C/C_0$) under varying pressure loads. As shown in Figure 6b, the sensor exhibits a characteristic bilinear response with two distinct linear regions, a high-sensitivity regime with a sensitivity of 0.67 kPa^{-1} in the low-pressure range (0–60 kPa) and a sensitivity of 0.16 kPa^{-1} in the high-pressure range (60–110 kPa). This high sensitivity at low pressures is attributed to the easily deformable nature of the eutectogel, which allows for a rapid increase in the effective contact area between the gel and electrodes upon initial compression. The sensor also demonstrates an ultrafast response speed, with a response time of 100 ms and a recovery time of 90 ms (Figure 6c), along with the capability to reliably distinguish between varying pressure levels of 3, 5, and 10 kPa (Figure 6d). The long-term durability was confirmed by Figure 6e, where the sensor maintained stable capacitive signals over 1000 continuous compression cycles, proving its resilience against mechanical fatigue. Leveraging these properties, the sensor was attached to the human throat and wrist to monitor physiological signals. It successfully captured the characteristic signal patterns of swallowing (Figure 6f) and radial artery pulses (Figure 6g). Notably, the high-fidelity pulse waveform in Figure 6h clearly displays the typical percussion, tidal, and dicrotic waves, highlighting the sensor's potential for cardiovascular health diagnosis. Beyond mechanical stimuli, the intrinsic hygroscopic nature of the DES endows the eutectogel with environmental humidity sensitivity. As displayed in Figure 6i, the resistance of the gel decreases significantly as the relative humidity (RH) increases from 45% to 75%, driven by the absorption of water molecules that enhances ionic mobility. The sensor exhibits excellent reversibility and speed when cyclically switched between 45% and 95% RH environments for two minutes (Figure 6j). Exploiting this humidity-responsive characteristic, the sensor was applied to non-contact respiration monitoring (Figure 6k). By detecting the moisture variations in exhaled (high humidity) and inhaled (low humidity) air, the sensor accurately recorded the user's breathing rate and depth, demonstrating its promise as a multi-functional wearable platform for comprehensive health tracking.

3 | Conclusion

In summary, we have successfully resolved the long-standing conflict between mechanical robustness and ionic conductivity in soft electronics by engineering a eutectogel featuring a stress-triggered ionic rearrangement mechanism. Structural analyses reveal that these exceptional properties originate from the formation of high-density amorphous ionic domains, which not only serve as robust sacrificial centers for energy dissipation but also enable a unique muscle-like self-strengthening behavior (185% enhancement) and outstanding fatigue resistance. Through the precise modulation of carboxyl ligand density and metal ion coordination, the optimized eutectogel achieves record-breaking mechanical properties, including a tensile strength of 34.58 MPa, a toughness of 177.3 MJ/m^3, and an elastic modulus of 77.38 MPa, while retaining a functional ionic conductivity of ~50 mS/m. Furthermore, the introduction of a deep eutectic solvent imparts the material with excellent anti-freezing tolerance down to −50°C. We demonstrated the practical versatility of this material through resistive sensors with an ultra-high gauge factor of 24.33 (detection limit ~10 μm) and capacitive sensors capable of multimodal physiological monitoring. This work establishes a promising paradigm for designing mechanically adaptive, environmentally stable, and highly sensitive ionic conductors for next-generation flexible electronics in extreme environments.

4 | Experimental Section

4.1 | Materials

Acrylamide (AM, C_3H_5NO), acrylic acid (AA, $C_3H_4O_2$), α-ketoglutaric acid ($C_5H_6O_5$), iron(III) chloride hexahydrate ($FeCl_3{\cdot}6H_2O$), choline chloride ($C_5H_{14}ClNO$), and ethylene

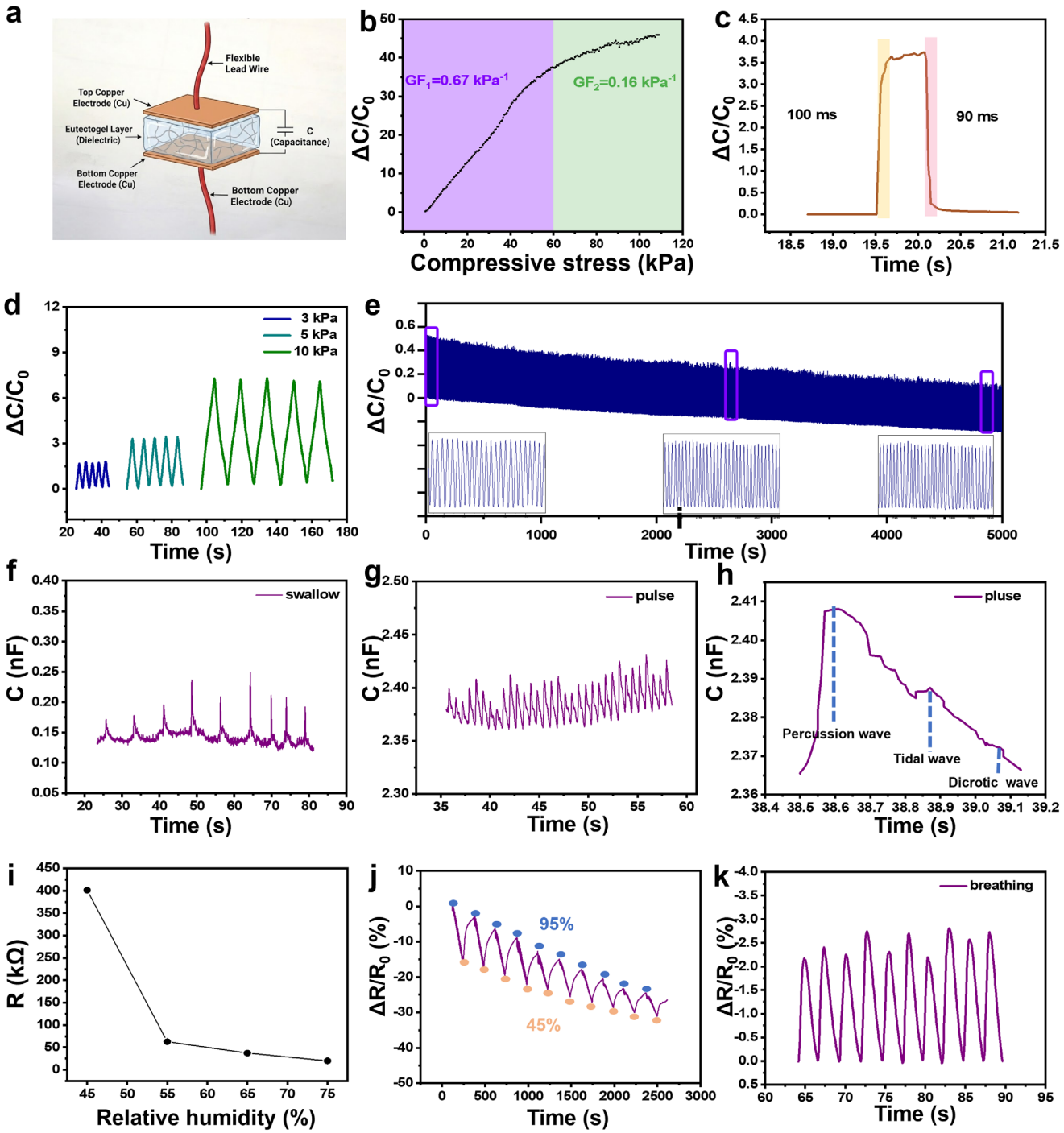

FIGURE 6 | Performance of the capacitive pressure sensor and environmental humidity responsiveness. (a) Schematic structure of the capacitive pressure sensor. (b) Relative capacitance changes versus compressive stress. (c) Ultrafast response and recovery times. (d) Precise distinction of varying pressure loads (3, 5, 10 kPa). (e) Long-term cyclic stability over 1000 compression cycles. Physiological signal monitoring applications such as (f) detection of throat swallowing motions and (g) real-time monitoring of radial artery pulses, with (h) a magnified waveform revealing characteristic pulse peaks (P, T, D waves). (i) Resistance variation as a function of relative humidity (RH). (j) Dynamic response and reversibility between 45% and 95% RH. (k) Non-contact respiration monitoring based on humidity changes in exhaled breath.

glycol ($C_2H_6O_2$) were purchased from Shanghai Aladdin Biochemical Technology Co., Ltd. (Shanghai, China). Deionized water (18.2 MΩ*cm) was used throughout the experiments. All chemical reagents were used as received without further purification.

4.2 | Preparation of High-Performance Conductive Eutectogels

The high-performance conductive eutectogels were synthesized using a systematic multi-step process involving free radical

polymerization, ionic coordination, and solvent displacement. First, to construct the polymer network, 3.0 g of acrylamide (AM), 0.01 g of α-ketoglutaric acid (photo-initiator), and varying amounts of acrylic acid (AA, ranging from 0.36 to 0.66 g) were dissolved in 10.0 mL of deionized water. The mixture was magnetically agitated at room temperature for 30 min to yield a homogeneous precursor solution. Subsequently, the solution was cast into a mold consisting of two acrylic plates separated by a 1.0 mm thick silicone rubber spacer and exposed to UV irradiation (365 nm) for 1 h, yielding a poly(acrylamide-*co*-acrylic acid) (P(AM-*co*-AA)) hydrogel. To introduce ionic cross-linking and optimize mechanical performance, the prepared hydrogels were immersed in iron (III) chloride ($FeCl_3$) solutions for 4 h. In the initial screening phase, the $FeCl_3$ concentration was fixed at 0.1 M for hydrogels with varying AA contents (0.36, 0.42, 0.48, 0.54, 0.60, and 0.66 g) to determine the optimal carboxyl density. Based on the resulting properties, the hydrogel containing 0.60 g of AA was selected as the optimal matrix, which was then immersed in $FeCl_3$ solutions with varying concentrations (0, 0.05, 0.10, 0.20, and 0.30 M) to further tune the coordination strength. Following the ionic coordination, the hydrogels were soaked in a deep eutectic solvent (DES) bath (choline chloride and ethylene glycol at a 1:1 mass ratio) for 12 h to facilitate solvent exchange. Finally, the eutectogels were removed and conditioned in air at ambient temperature (25°C, 80% humidity) for 24 h to reach thermodynamic equilibrium.

4.3 | Characterization and Biocompatibility

The chemical structures and intermolecular interactions of the synthesized gels were analyzed by Fourier transform infrared (FTIR) spectroscopy using a Thermo Scientific Nicolet iS 50 spectrometer equipped with an attenuated total reflection (ATR) attachment. The spectra were recorded over a wavenumber range of 4000–500 cm^{-1}. The surface morphology and elemental distribution of the freeze-dried samples were investigated using scanning electron microscopy (SEM) and energy-dispersive X-ray spectroscopy (EDS) on a TESCAN MIRA3 system. Before observation, the gel samples were lyophilized to preserve their porous structure. To probe the multi-scale hierarchical structure and the evolution of ionic domains, Small-Angle X-ray Scattering (SAXS) and Wide-Angle X-ray Scattering (WAXS) measurements were performed simultaneously using a Xeuss 3.0 system (Xenocs, France). The instrument was equipped with a Cu Kα radiation source (λ = 1.54 Å) and a solid-state detector. The scattering profiles were collected at room temperature, and the 2D scattering patterns were integrated into 1D curves as a function of the scattering vector q. The thermal properties and anti-freezing performance of the eutectogels were evaluated by differential scanning calorimetry (DSC) using a Mettler DSC3 instrument. The samples (approximately 5–10 mg) were sealed in aluminum pans and subjected to a cooling and heating cycle ranging from −60°C to 30°C at a rate of 5°C/min under a continuous nitrogen atmosphere flow. The native in situ 3D network morphology of the highly solvated samples, which prevents the artificial structural collapse typical of conventional freeze-drying, was visualized using cryogenic scanning electron microscopy (Cryo-SEM, Hitachi SU8010). To evaluate the dynamic mechanical properties and accurately determine the structural yield points of the networks under increasing deformation, rheological oscillatory strain sweeps were conducted using a rotational rheometer (TA Instruments HR-20), and polarized optical microscopy observations were performed using a Leica DM2500 microscope to capture the emergence of macroscopic birefringence and structural anisotropy.

To evaluate the cytotoxicity of the prepared eutectogels, a standard Cell Counting Kit-8 (CCK-8) assay was performed. Briefly, the target cells were seeded into 96-well culture plates at a predetermined density and incubated under standard physiological conditions with 5% CO2 for 24 h to allow for complete cell attachment. Subsequently, the original culture medium was replaced with the extraction media of the eutectogels or fresh medium containing different concentrations of the samples, and the cells were further cultured for 24 and 48 h. Following the designated incubation periods, a specific volume of the CCK-8 reagent was added to each well according to the manufacturer's protocol.

4.4 | Mechanical Testing

The mechanical properties of the eutectogels were evaluated via uniaxial tensile tests using a universal testing machine (Shanghai Lishi Instruments Co., Ltd., China) equipped with a 100 N load cell. To ensure standardized testing conditions and data reproducibility, the eutectogel samples were meticulously shaped into standard dumbbell specimens with precise gauge dimensions (gauge length: 12 mm, width: 2 mm) and a uniform thickness of approximately 1.0 mm. All tensile tests were conducted at a constant crosshead speed of 50 mm/min at room temperature. At least three replicates were tested for each experimental group to obtain average values. The engineering tensile stress (σ) was calculated by dividing the applied force by the initial cross-sectional area of the sample, while the tensile strain (ε) was determined by dividing the displacement by the initial gauge length. The elastic modulus (E), representing the stiffness of the network, was calculated as the slope of the stress–strain curve within the linear elastic region corresponding to 5%–10% strain. Furthermore, the toughness was quantified by integrating the area under the stress–strain curve until the point of fracture, representing the energy absorption capacity of the gels.

4.5 | Self-Recovery and Self-Strengthening Assessment

The dynamic mechanical behaviors, including fatigue resistance, self-recovery capability, and the time-dependent self-strengthening effect, were systematically evaluated using the same universal testing machine under cyclic loading conditions. To assess the anti-fatigue performance, the eutectogel samples were subjected to 200 continuous loading–unloading cycles at a fixed maximum strain (ε_{max}) of 100% without any resting interval between cycles. The stress–strain curves were recorded to monitor stress degradation and structural stability over long-term deformation. The self-recovery properties were investigated through interrupted cyclic tensile tests on eutectogels with varying Fe^{3+} concentrations. In this protocol, the samples were first stretched to 100% strain and unloaded. Subsequently, the samples were allowed to rest at room temperature for varying

intervals (1, 5, 30, and 60 min before being re-stretched to the same strain. The recovery efficiency was quantified by comparing the hysteresis energy (area of the loop) or maximum stress of the recovered cycle to that of the initial cycle. To quantify the self-strengthening effect, a specific time-resolved cyclic testing protocol was employed. The samples were subjected to loading–unloading cycles at a fixed strain of 100% at regular time intervals (every 30 min). The peak stress at 100% strain for each cycle was recorded and normalized against the initial stress to calculate the self-strengthening ratio, thereby elucidating the kinetics of the stress-triggered ionic rearrangement and network reconstruction. The self-recovery efficiency (η) was quantitatively evaluated using two metrics: the recovery of dissipated energy and the recovery of peak stress.

The energy recovery efficiency was calculated as $\eta_{\text{energy}} = (U_t/U_0) \times 100\%$, where U_0 and U_t represent the hysteresis loop areas (dissipated energy) of the first cycle and the re-loading cycle after a specific resting time, respectively. To quantify the time-dependent self-strengthening behavior, the ratio was calculated based on the peak stress variation: $\eta_s = (\sigma_t/\sigma_0) \times 100\%$, where σ_0 is the initial peak stress at 100% strain and σ_t is the peak stress measured after a resting interval of t. A value of $\eta_s > 100\%$ indicates a self-strengthening effect.

4.6 | Electrical Conductivity Measurements

The ionic conductivity of the eutectogels was quantitatively characterized using a precision LCR meter (Keysight E4980A) in resistance mode (R-X). To ensure accurate signal acquisition and minimize electrode polarization effects, the measurements were conducted under an alternating current (AC) voltage of 1.0 V at a fixed frequency of 1 kHz. The eutectogel samples were cut into standard dumbbell specimens with precise gauge dimensions (gauge length: 12 mm, width: 2 mm) and a uniform thickness of approximately 1.0 mm and sandwiched between two conductive electrodes. To guarantee data reliability and reproducibility, at least three independent specimens were tested for each composition, and the average values were recorded. The ionic conductivity (κ, mS/m) was calculated from the measured resistance (R, Ω) using the following equation:

$$\kappa = \frac{L}{RS}$$

where L denotes the distance between the two electrodes (i.e., the gauge length of the sample), and S represents the cross-sectional area perpendicular to the current flow.

4.7 | Application as Flexible Sensors

To explore the potential of the eutectogels in wearable electronics, the samples were fabricated into resistive strain sensors and capacitive pressure sensors to detect tensile deformation and compressive stress, respectively. For the resistive strain-sensing mode, the conductive eutectogel served as the sensing element. Fine copper wires were attached to both ends of the gel strip using silver paste and connected to the LCR meter. Copper wires were selected as interconnects due to their excellent conductivity and compliance, allowing them to accommodate large-scale deformations during stretching. For the capacitive pressure sensing mode, the eutectogel was sandwiched between two parallel copper plates. The rigidity of the copper plates ensured stable contact with the gel surface during compression, thereby minimizing contact resistance fluctuations and serving as current collectors. The electrical signals were recorded in real-time using the LCR meter (1 V, 1 kHz) while the mechanical deformation was precisely controlled by the universal testing machine (Shanghai Lishi Instruments Co., Ltd., China). The relative resistance change ($\Delta R/R_0$) was calculated as:

$$\frac{\Delta R}{R_0}\ (\%) = \frac{(R_t - R_0)}{R_0} \times 100\%$$

where R_0 and R_t denote the resistance values before and after applying strain, respectively. Similarly, for the capacitive mode, the relative capacitance change ($\Delta C/C_0$) was determined using the initial capacitance (C_0) and the real-time capacitance (C_t).

$$\frac{\Delta C}{C_0}\ (\%) = \frac{(C_t - C_0)}{C_0} \times 100\%$$

The resistive response was evaluated under hierarchical strain levels, including micro-strains (0.1%, 0.2%, and 0.25%), medium strains (1%, 2%, and 2.5%), and large strains (20%, 30%, and 50%). To assess durability, the sensors were subjected to 100 loading–unloading cycles at defined strains. The eutectogel sensors' sensitivity was the gauge factor (GF). It was calculated using the following equation:

$$GF = \frac{(Ri - R_0)/R_0}{\varepsilon}$$

The capacitive response was tested under varying compressive stresses and the long-term reliability was verified through 1000 continuous compression cycles. Given the hygroscopic nature of the DES, the environmental sensitivity was examined by exposing the sensors to relative humidity (RH) levels of 45%, 55%, 65%, and 75%. The dynamic response was further tested by cyclically switching the sensor between 45% and 95% RH environments. As a proof-of-concept demonstration, the assembled flexible sensors were directly attached to the skin of a volunteer using medical tape. Real-time electrical signals were recorded to monitor various physiological activities, ranging from large-scale limb movements to subtle physiological signals such as swallowing and pulse.

Acknowledgements

The work was funded by the Basic Research Program of Shenzhen (JCYJ20230807093559046), National Natural Science Foundation of China (92471203).

Conflicts of Interest

The authors declare no conflicts of interest.

Data Availability Statement

The data that support the findings of this study are available from the corresponding author upon reasonable request.

References

1. J. J. Wei, P. Xiao, and T. Chen, "Water-Resistant Conductive Gels toward Underwater Wearable Sensing," *Advanced Materials* 35 (2023): e2211758, https://doi.org/10.1002/adma.202211758.

2. Y. Liu, W. Z. Zou, N. Zhao, and J. Xu, "Electrically Insulating PBO/MXene Film With Superior Thermal Conductivity, Mechanical Properties, Thermal Stability, and Flame Retardancy," *Nature Communications* 14, no. 9 (2023): 5342, https://doi.org/10.1038/s41467-023-40707-x.

3. L. Y. Lan, J. F. Ping, H. Y. Li, et al., "Skin-Inspired All-Natural Biogel for Bioadhesive Interface," *Advanced Materials* 36 (2024): e2401151, https://doi.org/10.1002/adma.202401151.

4. T. Li, H. B. Qi, C. C. Zhao, et al., "Robust Skin-Integrated Conductive Biogel for High-Fidelity Detection Under Mechanical Stress," *Nature Communications* 16, no. 15 (2025): 88, https://doi.org/10.1038/s41467-024-55417-1.

5. H. B. Ma, M. Wang, J. W. Hou, X. L. Wang, P. C. Sun, and F. F. Wang, "Strong and Tough Water-Tolerant Conductive Eutectogels With Phase-Separated Hydrophilic/Hydrophobic Dual Ionic Channels," *Advanced Materials* 37, no. 13 (2025): 2500770, https://doi.org/10.1002/adma.202500770.

6. Z. Y. Liu, T. Liu, H. P. Dong, et al., "Diatom-Inspired Nanoscale Heterogeneous Assembly Strategy for Constructing Thermal Insulating Wood-Based Aerogels With Exceptional Strength, Resilience, Degradability, and Flame Retardancy," *ACS Nano* 19 (2025): 6826–6839, https://doi.org/10.1021/acsnano.4c11549.

7. S. L. Zhang, J. Y. Wang, L. L. Li, et al., "Highly Compressible Wide-Frequency Region Dissipative Ionogels Resistant to High Strain Rate Impact," *Advanced Functional Materials* 36 (2026): e31978, https://doi.org/10.1002/adfm.202531978.

8. X. T. Wang, N. Tang, Y. J. Jiang, M. H. Li, and J. Hu, "Copper-Coordination Engineered Glassy Hydrogels Featuring Ultrastiffness and Structural Programmability," *Small* 21 (2025): e2502949, https://doi.org/10.1002/smll.202502949.

9. L. C. Geonzon, J. Chan, H. Kou, et al., "Tough and Stiff Biobased Hydrogels Reinforced by Strain-Induced Ordering of Hierarchical Structure," *Chemistry of Materials* 37 (2025): 6991–7001, https://doi.org/10.1021/acs.chemmater.5c00790.

10. Z. J. Wang, W. Li, X. Y. Li, T. Nakajima, M. Rubinstein, and J. P. Gong, "Rapid Self-strengthening in Double-network Hydrogels Triggered by Bond Scission," *Nature Materials* 24 (2025): 607–614, https://doi.org/10.1038/s41563-025-02137-6.

11. E. Howard, M. H. Li, M. Kozma, J. Y. Zhao, and J. Bae, "Self-Strengthening Stimuli-Responsive Nanocomposite Hydrogels," *Nanoscale* 14 (2022): 17887–17894, https://doi.org/10.1039/D2NR05408F.

12. B. K. Bao, Q. M. Zeng, K. Li, et al., "Rapid Fabrication of Physically Robust Hydrogels," *Nature Materials* 22 (2023): 1253–1260, https://doi.org/10.1038/s41563-023-01648-4.

13. L. X. Hou, H. Q. Ju, X. P. Hao, et al., "Intrinsic Anti-Freezing and Unique Phosphorescence of Glassy Hydrogels with Ultrahigh Stiffness and Toughness at Low Temperatures," *Advanced Materials* 35 (2023): 2300244, https://doi.org/10.1002/adma.202300244.

14. J. P. Gong, Y. Katsuyama, T. Kurokawa, and Y. Osada, "Double-Network Hydrogels With Extremely High Mechanical Strength," *Advanced Materials* 15 (2003): 1155–1158, https://doi.org/10.1002/adma.200304907.

15. H. Tsukeshiba, M. Huang, Y. H. Na, et al., "Effect of Polymer Entanglement on the Toughening of Double Network Hydrogels," *The Journal of Physical Chemistry B* 109 (2005): 16304–16309, https://doi.org/10.1021/jp052419n.

16. X. Guo, X. Y. Dong, G. J. Zou, H. J. Gao, and W. Zhai, "Strong and Tough Fibrous Hydrogels Reinforced by Multiscale Hierarchical Structures With Multimechanisms," *Science Advances* 9, no. 12 (2023): adf7075, https://doi.org/10.1126/sciadv.adf7075.

17. M. T. Hua, S. W. Wu, Y. F. Ma, et al., "Strong Tough Hydrogels via the Synergy of Freeze-Casting and Salting Out," *Nature* 590, no. 13 (2021): 594–599, https://doi.org/10.1038/s41586-021-03212-z.

18. R. X. Zhu, D. D. Zhu, Z. Zheng, and X. L. Wang, "Tough Double Network Hydrogels With Rapid Self-Reinforcement and Low Hysteresis Based on Highly Entangled Networks," *Nature Communications* 15, no. 11 (2024): 1344, https://doi.org/10.1038/s41467-024-45485-8.

19. J. H. Kang, X. Z. Su, P. P. Zhou, et al., "Supramolecular Interlocking Produces Mechanically Anisotropic, Robust, and Tough Biomimetic Ionogels," *Advanced Materials* 38 (2026): e11903, https://doi.org/10.1002/adma.202511903.

20. M. T. I. Mredha, Y. Z. Guo, T. Nonoyama, T. Nakajima, T. Kurokawa, and J. P. Gong, "A Facile Method to Fabricate Anisotropic Hydrogels With Perfectly Aligned Hierarchical Fibrous Structures," *Advanced Materials* 30, no. 8 (2018): 1704937, https://doi.org/10.1002/adma.201704937.

21. Y. Z. Liang, D. D. Zou, Y. H. Zhang, and Z. Zhong, "Indirect Method for Preparing Dual Crosslinked Eutectogels With High Strength, Stretchability, Conductivity and Rapid Self-Recovery Capability as Flexible and Freeze-Resistant Strain Sensors," *Chemical Engineering Journal* 475, no. 12 (2023): 145928, https://doi.org/10.1016/j.cej.2023.145928.

22. Y. Z. Liang, L. Q. Lin, H. Y. Liang, and Z. Zhong, "Longevous Ionogels With High Strength, Conductivity, Adhesion and Thermoplasticity," *Chemical Engineering Journal* 497, no. 13 (2024): 155047, https://doi.org/10.1016/j.cej.2024.155047.

23. M. X. Wang, X. Xiao, S. Siddika, et al., "Glassy Gels Toughened by Solvent," *Nature* 631 (2024): 313–318, https://doi.org/10.1038/s41586-024-07564-0.

24. W. Z. Li, X. L. Wang, Z. Y. Liu, et al., "Nanoconfined Polymerization Limits Crack Propagation in Hysteresis-Free Gels," *Nature Materials* 23 (2024): 131–138, https://doi.org/10.1038/s41563-023-01697-9.

25. X. Sun, Y. M. Mao, Z. Y. Yu, P. Yang, and F. Jiang, "A Biomimetic "Salting Out—Alignment—Locking" Tactic to Design Strong and Tough Hydrogel," *Advanced Materials* 36, no. 9 (2024): 2400084.

26. Q. Y. Liu, X. Y. Dong, H. B. Qi, et al., "3D Printable Strong and Tough Composite Organo-Hydrogels Inspired by Natural Hierarchical Composite Design Principles," *Nature Communications* 15, no. 11 (2024): 3237, https://doi.org/10.1038/s41467-024-47597-7.

27. B. Xue, Z. Bashir, Y. C. Guo, et al., "Strong, Tough, Rapid-Recovery, and Fatigue-Resistant Hydrogels Made of Picot Peptide Fibres," *Nature Communications* 14, no. 10 (2023): 2583, https://doi.org/10.1038/s41467-023-38280-4.

28. L. L. Chen, Z. K. Jin, W. W. Feng, L. Sun, H. Xu, and C. Wang, "A Hyperelastic Hydrogel With an Ultralarge Reversible Biaxial Strain," *Science* 383 (2024): 1455–1461, https://doi.org/10.1126/science.adh3632.

29. Y. Jiang, D. Z. Zhan, M. Zhang, et al., "Strong and Ultra-tough Ionic Hydrogel Based on Hyperbranched Macro-Cross-linker: Influence of Topological Structure on Properties," *Angewandte Chemie International Edition* 62, no. 12 (2023): 202310832, https://doi.org/10.1002/anie.202310832.

30. M. X. Wang, P. Y. Zhang, M. Shamsi, et al., "Tough and Stretchable Ionogels by In Situ Phase Separation," *Nature Materials* 21 (2022): 359–365, https://doi.org/10.1038/s41563-022-01195-4.

31. N. Tang, Y. J. Jiang, K. L. Wei, Z. R. Zheng, H. Zhang, and J. Hu, "Evolutionary Reinforcement of Polymer Networks: A Stepwise-Enhanced Strategy for Ultrarobust Eutectogels," *Advanced Materials* 36 (2024): 2309576, https://doi.org/10.1002/adma.202309576.

32. Y. H. Fang, C. Liang, V. Liljeström, Z. P. Lv, O. Ikkala, and H. Zhang, "Toughening Hydrogels With Fibrillar Connected Double Networks," *Advanced Materials* 36, no. 11 (2024): 2402282.

33. Y. C. Wu, Y. Zhang, H. D. Wu, et al., "Solvent-Exchange-Assisted Wet Annealing: A New Strategy for Superstrong, Tough, Stretchable, and Anti-Fatigue Hydrogels," *Advanced Materials* 35, no. 11 (2023): 2210624.

34. L. L. Li, W. Z. Li, X. L. Wang, et al., "Ultra-Tough and Recyclable Ionogels Constructed by Coordinated Supramolecular Solvents," *Angewandte Chemie International Edition* 61 (2022): 11.

35. J. F. Xiong, X. W. Wang, L. L. Li, et al., "Low-Hysteresis and High-Toughness Hydrogels Regulated by Porous Cationic Polymers: The Effect of Counteranions," *Angewandte Chemie International Edition* 63, no. 9 (2024): 202316375, https://doi.org/10.1002/anie.202316375.

36. G. G. Zhang, J. Steck, J. Kim, C. H. Ahn, and Z. G. Suo, "Hydrogels of Arrested Phase Separation Simultaneously Achieve High Strength and Low Hysteresis," *Science Advances* 9, no. 7 (2023): adh7742, https://doi.org/10.1126/sciadv.adh7742.

37. Z. Wang, X. J. Zheng, T. Ouchi, et al., "Toughening Hydrogels Through Force-Triggered Chemical Reactions that Lengthen Polymer Strands," *Science* 374 (2021): 193–196, https://doi.org/10.1126/science.abg2689.

38. C. Liu, N. Morimoto, L. Jiang, et al., "Tough Hydrogels With Rapid Self-Reinforcement," *Science* 372 (2021): 1078–1081, https://doi.org/10.1126/science.aaz6694.

39. Y. K. Shi, B. H. Wu, S. T. Sun, and P. Y. Wu, "Aqueous Spinning of Robust, Self-Healable, and Crack-Resistant Hydrogel Microfibers Enabled by Hydrogen Bond Nanoconfinement," *Nature Communications* 14, no. 13 (2023): 1370, https://doi.org/10.1038/s41467-023-37036-4.

40. S. J. Wu, C. H. Gong, Z. C. Wang, et al., "Continuous Spinning of High-Tough Hydrogel Fibers for Flexible Electronics by Using Regional Heterogeneous Polymerization," *Advancement of Science* 10 (2023): 2305226, https://doi.org/10.1002/advs.202305226.

41. Y. Wang, Q. Y. Zhou, D. W. Wang, Q. Q. Liu, X. P. Zeng, and J. Y. Wu, "High-Strength, Dual-Responsive Conductive Hydrogels With Ionic Crosslinking for Flexible Strain Sensors," *Journal of Polymer Science* 63 (2025): 2834–2845, https://doi.org/10.1002/pol.20250279.

42. C. G. Xu, A. Xie, H. Y. Hu, et al., "Ultrastrong Eutectogels Engineered via Integrated Mechanical Training in Molecular and Structural Engineering," *Nature Communications* 16, no. 13 (2025): 2589, https://doi.org/10.1038/s41467-025-57800-y.

Supporting Information

Additional supporting information can be found online in the Supporting Information section.

Supporting File: adfm76284-sup-0001-SuppMat.docx.